RELATIVISTIC ELECTRON SHOCK DRIFT ACCELERATION IN LOW MACH NUMBER GALAXY CLUSTER SHOCKS

Matsukiyo, Shuichi
Department of Earth System Science and Technology, Kyushu University

Ohira, Yutaka
High Energy Acceleration Research Organization

Yamazaki, Ryo
Department of Physics and Mathematics, Aoyama Gakuin University

Umeda, Takayuki
Solar-Terrestrial Environment Laboratory, Nagoya University

https://hdl.handle.net/2324/20259

出版情報：Astrophysical Journal. 742, pp.47-1-47-9, 2011-11-03. The American Astronomical Society
バージョン：

The Astrophysical Journal, 742:47 (9pp), 2011 November 20 doi:10.1088/0004-637X/742/1/47

RELATIVISTIC ELECTRON SHOCK DRIFT ACCELERATION IN LOW MACH NUMBER GALAXY CLUSTER SHOCKS

S. Matsukiyo[1], Y. Ohira[2], R. Yamazaki[3], and T. Umeda[4]
[1] Department of Earth System Science and Technology, Kyushu University, Kasuga,
Fukuoka 816-8580, Japan; matsukiy@esst.kyushu-u.ac.jp
[2] High Energy Acceleration Research Organization, Tsukuba,
Ibaraki 305-0801, Japan; ohira@post.kek.jp
[3] Department of Physics and Mathematics, Aoyama Gakuin University, Sagamihara,
Kanagawa 252-5258, Japan; ryo@phys.aoyama.ac.jp
[4] Solar-Terrestrial Environment Laboratory, Nagoya University, Nagoya,
Aichi 464-8601, Japan; umeda@stelab.nagoya-u.ac.jp
Received 2011 April 5; accepted 2011 August 23; published 2011 November 3

ABSTRACT

An extreme case of electron shock drift acceleration (SDA) in low Mach number collisionless shocks is investigated as a plausible mechanism for the initial acceleration of relativistic electrons in large-scale shocks in galaxy clusters, where the upstream plasma temperature is of the order of 10 keV and the degree of magnetization is not too small. One-dimensional electromagnetic full particle simulations reveal that, even when a shock is rather moderate, a part of the thermal incoming electrons are accelerated and reflected through relativistic SDA and form a local non-thermal population just upstream of the shock. The accelerated electrons can self-generate local coherent waves and further be back-scattered toward the shock by those waves. This may be a scenario for the first stage of the electron shock acceleration occurring at the large-scale shocks in galaxy clusters, such as CIZA J2242.8+5301, which have well-defined radio relics.

Key words: acceleration of particles – galaxies: clusters: general – plasmas – radio continuum: galaxies – relativistic processes – shock waves

Online-only material: color figures

1. INTRODUCTION

In galaxy clusters, the presence of relativistic electrons with energies of around GeV has been implied by radio synchrotron emission (e.g., Willson 1970; Govoni & Feretti 2004; Fujita & Sarazin 2001). Although some possible acceleration mechanisms for those relativistic electrons have been proposed, they are still controversial topics (for a recent review, see Ferrari et al. 2008). The diffuse radio emission in galaxy clusters is categorized into several types, such as jet robes from active galactic nuclei, radio halos located at the center of galaxy clusters, and radio relics located at the cluster periphery. In particular, the origin of radio relics has been a major mystery. Recent observations suggest that they are associated with large-scale shocks, which are also thought to be possible sources of the ultra-high-energy cosmic rays above $\approx 10^{18.5}$ eV (Kang et al. 1997; Inoue et al. 2007). The existence of shocks in the radio relics implies that the high-energy electrons are most likely produced through the diffusive shock acceleration process (Enßlin et al. 1998; Miniati et al. 2001; Gabici & Blasi 2003; Keshet et al. 2004). In fact, radio shells showing the spectral softening due to the synchrotron and the inverse-Compton coolings are observed in CIZA J2242.8+5301 (van Weeren et al. 2010), while a temperature jump is found in A3667 (Finoguenov et al. 2010). Observations suggest that the temperature is $T \approx 9$ keV, the magnetic field strength is $B \approx 5\,\mu$G, and the Mach number is $M \approx 4.5$ for CIZA J2242.8+5301, and $T \approx 2$–5 keV, $B \gtrsim 3\,\mu$G, $M \approx 2$, and the number density is $n \approx 10^{-5}$–10^{-4} for A3667.

According to the standard theory of structure formation, galaxy clusters result from mergers of smaller structures. High Mach number shocks ($M > 10$) are formed in accreting small halos and around the virialized core of the galaxy cluster. They can accelerate cosmic rays to ultra-high energies with a harder energy spectrum. On the other hand, low Mach number shocks ($M < 10$) are formed in the virialized core. During the mergers and accretions, the most kinetic energy of the accreting matter is dissipated by relatively low Mach number shocks with $M \lesssim 4$ (Miniati et al. 2000; Ryu et al. 2003; Kang et al. 2007). These shocks with $M \approx 3$–4 are needed in order to explain spectral indices of radio relics (Gabici & Blasi 2003). In fact, the shock velocity in the radio relics of the galaxy cluster is of the order of 10^3 km s^{-1} and the corresponding Mach numbers are about $M \approx 2$–4.5 (van Weeren et al. 2010; Finoguenov et al. 2010). The shock velocity is similar to what is observed for young supernova remnant (SNR) shocks, which generate galactic cosmic-ray electrons (Koyama et al. 1995) as well as nuclei (e.g., Ohira et al. 2011). However, the Mach number of a galaxy cluster shock is much smaller than that of an SNR shock because of a high upstream temperature as well as the so-called magnetization parameter, $\sigma \equiv B_1^2/4\pi n_1 m_e c^2$. Here, B_1, n_1, m_e, and c denote upstream magnetic field, plasma density, electron rest mass, and the speed of light, respectively. Then, for the galaxy clusters, $T \approx 1$–10 keV and $\sigma \sim 0.1$ with $B_1 = 3\,\mu$G and $n_1 = 10^{-4}$ cm^{-3}. Such small values of Mach numbers are of the same order as those of the shocks observed in the heliosphere, i.e., the terrestrial bow shock and interplanetary shocks in which electron acceleration is rarely observed (Shimada et al. 1999; Oka et al. 2006, 2009).

The diffusive shock acceleration is one of the most plausible acceleration mechanisms of charged particles at a shock front (e.g., Blandford & Eichler 1987), where a resultant energy spectrum of the high-energy particles obeys a power law. For SNR shocks, galactic cosmic rays are thought to be accelerated through this process. It is not resolved, however, as to how a part of the particles originally composing a thermal background plasma is embedded in the diffusive shock acceleration, which requires the preexistence of non-thermal particles to flow freely over the shock. This is the so-called injection problem on the diffusive shock acceleration. In general, electron injection is thought to be more difficult than ion injection because of cross-shock potential. Nevertheless, relativistic electrons are believed to be accelerated in SNR shocks (Koyama et al. 1995; Bamba et al. 2003; Pannuti et al. 2010). Although a variety of theoretical as well as simulation studies have revealed that microinstabilities in the shock transition region play some crucial roles, the electron injection process, even in extremely high Mach number shocks, has not yet been understood completely (e.g., Papadopoulos 1988; Cargill & Papadopoulos 1988; Levinson 1992; Shimada & Hoshino 2000; Dieckmann et al. 2000; Hoshino & Shimada 2002; Ohira & Takahara 2007, 2008; Umeda et al. 2008, 2009; Amano & Hoshino 2007, 2009, 2010; Morlino 2009; Riquelme & Spitkovsky 2010).

In the above context, electron injection in low Mach number shocks is inferred to be even harder, since the free energy for microinstabilities in the shock transition region should be much smaller than that in high Mach number shocks. Although a variety of microinstabilities get excited in some heliospheric shocks (e.g., Wu et al. 1984), it is known, for instance, that the saturation level of the modified two-stream instability, which is one of the most plausible instabilities in shocks observed near the Earth, is not as high as that of the Buneman instability in SNR shocks (Matsukiyo 2010). Given this perspective, an injection process of electrons in the galaxy cluster shocks is shrouded in mystery. Indeed, this problem has never been addressed. Here, we note that the upstream temperature of the cluster shocks is much higher than those of SNR and heliospheric shocks. As can be seen in the next section, the high upstream temperature enables some electrons to be accelerated to relativistic energies via the so-called shock drift acceleration (SDA).

In this paper, we investigate a limiting case of the electron SDA and associated microprocesses which may be responsible for the injection of electrons into the diffusive shock acceleration in the galaxy cluster shocks. In Section 2, the SDA process is briefly reviewed and extended to an extreme case. Simulation settings and results are shown in Section 3. Then, discussions and a summary are given in Section 4.

2. SHOCK DRIFT ACCELERATION

2.1. Some Basic Features

SDA is one of the efficient acceleration mechanisms of charged particles in the transition region of an oblique collisionless shock. The motion of non-relativistic electrons in this process was analyzed in detail previously (e.g., Leroy & Mangeney 1984; Wu 1984; Krauss-Varban et al. 1989; Krauss-Varban & Wu 1989; Krauss-Varban & Burgess 1991). In the so-called normal incidence frame (NIF), where the upstream flow direction is parallel to a shock normal, the acceleration occurs while an electron stays in the shock transition region and drifts along the shock surface due to a finite gradient of magnetic field strength. The electron gains energy since the direction of the drift motion is anti-parallel to the motional electric field.

Assuming that the coplanar magnetic field for a one-dimensional shock is in the x–z plane and the shock normal is along the x-axis, then

$$\dot{\gamma} = \frac{\mathbf{p}\cdot\dot{\mathbf{p}}}{m_0^2c^2\gamma} = -\frac{e}{m_ec^2}\mathbf{v}\cdot\mathbf{E} = -\frac{e}{m_ec^2}\left(-\dot{x}\frac{\partial\phi}{\partial x} + v_yE_0\right). \tag{1}$$

Here, γ, $\mathbf{p}$, $\mathbf{v}$, and e are the Lorentz factor, momentum, velocity and elementary charge, respectively, $\mathbf{E}$ is the electric field, and the dots denote the time derivative. Furthermore, $\mathbf{E} = (-\partial\phi/\partial x, E_0, 0)$ has been used, where ϕ and E_0 denote shock potential and the motional electric field. This results in

$$\dot{W} \equiv \frac{d}{dt}\left(\gamma - \frac{e\phi}{m_ec^2}\right) = -\frac{e}{m_ec^2}v_yE_0. \tag{2}$$

Some incoming electrons gain significant energy during the drift motion and are reflected backward from the shock. These reflected electrons become a non-thermal component in the upstream plasma frame. The reflection occurs due to the magnetic mirror effect. The de Hoffmann–Teller frame (HTF), where the upstream flow is along the magnetic field, is convenient to consider the motion of a particle because the motional electric field disappears in this frame. The particle velocity in HTF ($\mathbf{v}'$) and NIF ($\mathbf{v}$) is related as $\mathbf{v}' = \mathbf{v} + \mathbf{V_{HT}}$, where $\mathbf{V_{HT}} = (\mathbf{V_1}\times\mathbf{B_1})\times\hat{\mathbf{n}}/(\mathbf{B_1}\cdot\hat{\mathbf{n}})$ is the de Hoffmann–Teller velocity, $\hat{\mathbf{n}}$ is the unit vector normal to the shock, and $\mathbf{V_1}$ and $\mathbf{B_1}$ are the upstream flow velocity and the magnetic field in the NIF, respectively. In the HTF, the right-hand side of Equation (2) becomes zero so that W' is conserved. Moreover, if the motion of the electron is assumed to be adiabatic, magnetic moment, $\mu' = p'^2_\perp/2m_eB'$, is also conserved. Here, the prime denotes a quantity measured in the HTF. This assumption is valid while the spatial scale of a shock transition region is sufficiently larger than the Larmor radius of the electron. From these two restrictions, in order for the electron to be mirror reflected, the initial pitch angle, $\alpha'_1 = \tan^{-1}(p'_{1\perp}/p'_{1\parallel})$, should satisfy the following condition (cf. Feldman et al. 1983 for a non-relativistic version):

$$\alpha'_1 > \sin^{-1}\sqrt{\frac{B'_1}{B'_2}\,\frac{(\gamma'_1+\Delta\Phi')^2-1}{u'^2_1}}. \tag{3}$$

Here, B' denotes the magnetic field strength, $u' = p'/m_ec$, $\Delta\Phi' = e(\phi'_2 - \phi'_1)/m_ec^2$, and the subscripts 1 and 2 indicate upstream (initial) and downstream quantities, respectively. If an overshoot exists, however, B'_2 and ϕ'_2 should be defined there.

The energy gain in the SDA process is obtained by integrating Equation (2) in the NIF, $m_ec^2W(t) = -e\int E_0dy$, as the energy gained by an electron during its drift in the transition region along the direction anti-parallel to the motional electric field (for details see Krauss-Varban & Wu 1989). If one moves in the HTF, the energy gain is explained by the well-known Fermi acceleration mechanism (Wu 1984). If a particle velocity, before it's reflected, is written as $\mathbf{v}_{\rm pre}$, $\mathbf{v}'_{\rm pre} = \mathbf{v}_{\rm pre} + \mathbf{V_{HT}}$, then after being reflected, the parallel velocity is reversed so that $\mathbf{v}'_{\rm post} = (-v'_{\parallel,pre}, \mathbf{v}'_{\perp,\mathbf{pre}})$. Then, moving back in the NIF results in $\mathbf{v}_{\rm post} = \mathbf{v}'_{\rm post} - \mathbf{V_{HT}}$. Now, $\mathbf{V_{HT}} = (0, 0, U_1\tan\Theta_{Bn})$ when $\mathbf{V_1} = U_1\hat{\mathbf{n}}$ and $\hat{\mathbf{n}}$ is along the x-axis. Hence, the acceleration occurs mainly in the z-direction. The more $V_{\rm HT}$ increases, the larger the energy gain of the particle becomes. According to Krauss-Varban et al. (1989), the acceleration time through this process is typically of the order of an ion gyro period, $\sim\Omega_i^{-1}$, which will also be confirmed in our simulation later. For a typical intra-cluster magnetic field of μG, this corresponds to about a few 100 s, which is of course much shorter than any timescales of incoherent loss processes.

If $\Delta\Phi' = 0$ is assumed, $\alpha'_1 > \alpha'_c \equiv \sin^{-1}(B'_1/B'_2)^{1/2}$ is the necessary condition for an electron to be reflected. When a magnetic overshoot is neglected for simplicity, B'_2 or the critical pitch angle called a loss-cone angle, α'_c, can be determined

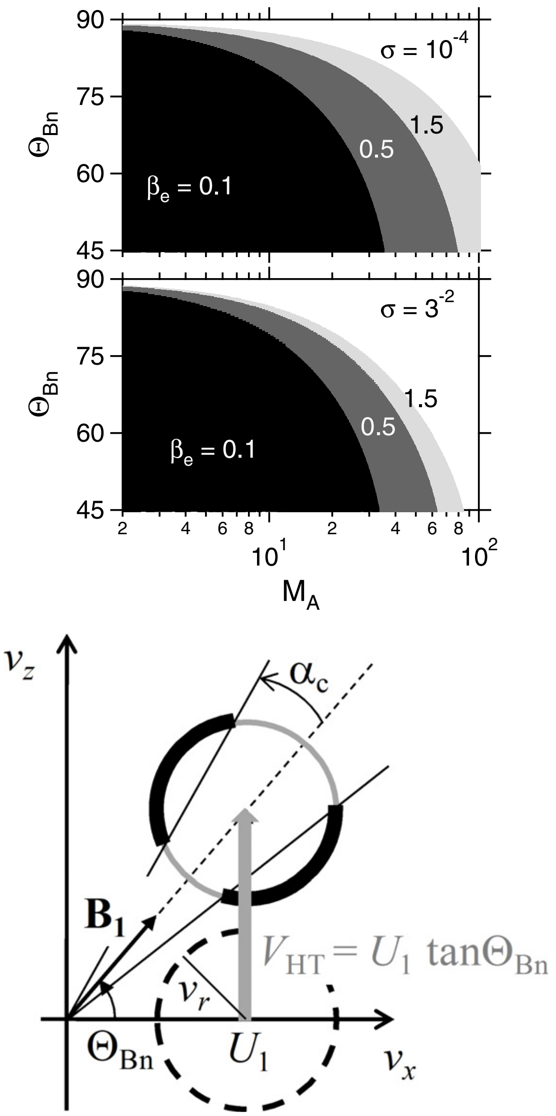

Figure 1. Feasibility of SDA. The top two panels show $M_A - \Theta_{Bn}$ parameter spaces where adiabatic electron reflection is possible for three different upstream electron beta values with $\sigma = 10^{-4}$ (top panel) and $\sigma = 3^{-2}$ (middle panel). The bottom panel shows a schematic of a loss-cone in the $v_z - v_x$ space.

from the Rankine–Hugoniot relation by giving a Mach number (M_A), an upstream plasma beta ($\beta = 8\pi n_1(T_e + T_i)/B_1^2$), and a shock angle ($\Theta_{Bn}$), which is the angle between the shock normal and upstream magnetic field (Tidman & Krall 1971). The top two panels in Figure 1 show regions in the $M_A - \Theta_{Bn}$ parameter space where some electrons on a velocity shell with a radius of $3v_{te}$ in an upstream plasma frame of the NIF can be reflected, where v_te is upstream electron thermal velocity. In the two panels, for instance in the black area, some electrons on such a velocity shell, corresponding to upstream electron beta ($\beta_e = 8\pi n_1 T_e/B_1^2$), being equal to 0.1 satisfy the condition $\alpha'_1 > \alpha'_c$, where $T_i = T_e$ has been assumed to calculate α'_c. Similarly, in the dark (light) gray area some electrons can be additionally reflected by assuming $\beta_e = 0.5(1.5)$. The top (middle) panel corresponds to the case with $\sigma = 10^{-4}(3^{-2})$. The figure confirms that the electrons are hardly reflected when M_A and/or Θ_{Bn} become too large. This may be graphically understood as follows. Suppose a velocity shell in the $v_z - v_x$ space is indicated as the broken circle in the bottom panel. Its center corresponds to the bulk velocity of the upstream plasma in the NIF, $(U_1, 0)$, and the radius of the shell is v_r. Let us consider whether or not some electrons on this velocity shell are mirror reflected (in this schematic picture, relativistic distortion of the shell has been neglected). If $V_{\rm HT}$ is added in v_z, the center of the shell shifts along the thick gray vertical arrow. Now a broken line connecting the origin with the new center of the shell is parallel to an upstream bulk velocity in the HTF, which is along the upstream magnetic field, $\mathbf{B_1}$. Two solid lines symmetrical with respect to the broken line denote a loss-cone. Therefore, the electrons outside this loss-cone indicated by the black solid arcs can be reflected or otherwise transmitted. When U_1 or a Mach number increases, the center of the shell shifts along the broken line and finally a whole shell lies inside the loss-cone. In this case no electrons are reflected. Similarly, when Θ_{Bn} becomes large, the broken line gets more vertical and the center of the shell walks away from the origin. Then the whole shell again enters a loss-cone. The possible reflection areas indicated in the top two panels are defined like this by assuming the shell radius $v_r = 3v_{te}$. The area expands with increasing β_e as expected. On the other hand, it does not depend much on σ. In particular when $\sigma < 10^{-3}$, distributions of the areas are almost exactly the same as the top panel. It is mainly due to the light speed limit of a shell radius that the areas look contracted for $\sigma = 3^{-2}$ in the middle panel, because increasing σ with constant β_e results in an increase of the thermal velocity. (The actual calculation is performed by taking relativistic effects into account so that the shell is given in momentum space with $p_r = 3p_{te}$.) It is speculated that in extremely high Mach number shocks, like an SNR shock whose Mach number is typically $M_A \sim 10^{2-3}$, electron reflection hardly occurs unless there are no preheating mechanisms as discussed by Amano & Hoshino (2007, 2010). On the other hand, electrons can be relatively easily reflected when $M_A < 10$, although acceleration may be weak because of small $V_{\rm HT}$. In practice, one should note that the finite shock potential may reduce the reflection rate (Wu 1984).

2.2. *An Extreme Case*

As mentioned above, in low Mach number shocks ($M_A < 10$) electrons are relatively easily reflected, although the resultant acceleration is not so efficient in general. However, if there are some electrons on the velocity shell with sufficiently large v_r, they may be reflected even at large Θ_{Bn} where $V_{\rm HT} \sim O(c)$. The reflected electron energy in such a case would become relativistic.

The condition that an upstream electron on a velocity shell with radius v_r can be reflected is $v'_r > (\sqrt{V_{\rm HT}^2 + U_1^2})' \sin\alpha'_c$. When $V_{\rm HT} \gg U_1$, this leads to $v'_r > V_{\rm HT}\sqrt{B'_1/B'_2}$, where the effects of shock potential have been again neglected. If $v_r = \eta v_{te}$, the following condition is finally obtained:

$$\eta > \eta_c \equiv \frac{U_1 \tan\Theta_{Bn}}{c}\left(\frac{B_1/B_2}{\beta_e\sigma/2}\right)^{1/2}. \qquad (4)$$

The inequality (4) implies that reflected electrons can be present if there are some electrons on a velocity shell with $v_r > \eta_c v_{te}$. The reflected electrons will have relativistic energies when $V_{\rm HT} = U_1 \tan\Theta_{Bn} \sim O(c)$. In this limit $\eta_c \to \eta_r$, where

$$\eta_r = \left(\frac{B_1/B_2}{\beta_e\sigma/2}\right)^{1/2} = \frac{\sqrt{B_1/B_2}}{v_{te}/c}. \qquad (5)$$

In the solar wind or interstellar plasmas η_r is extremely large, since the electron temperature is ∼100 eV at the highest and

Table 1
Shock Parameters

Run	M_A	M_f	U_1/c	σ	$\beta_e = \beta_i$	T_e (keV)	m_i/m_e	Θ_{Bn}	B_{os}/B_1	η_c
A	7.8	2.9	0.061	1/9	1.5	42.6	1836	85	6	0.99
B	7.7	2.9	0.060	1/9	1.5	42.6	1836	80	6	0.48
C	7.4	2.8	0.058	1/9	1.5	42.6	1836	60	6	0.14
D	5.0	1.9	0.029	1/16	1.5	24.0	1836	87	3.5	1.4

$\sigma \sim 10^{-(4-6)}$ ($\beta_e \sim O(1)$). Therefore, satisfying the above condition for a shock in an environment such as in Earth's bow shock or SNR shocks is almost hopeless. However, it may be possible if the electron temperature becomes ~10 keV or $\sigma \sim 10^{-(1-2)}$ and $\beta_e \sim 0.1$–1 as in some large-scale shocks in galaxy clusters (van Weeren et al. 2010; Nakar et al. 2008; Fujita et al. 2007).

3. ONE-DIMENSIONAL PIC SIMULATION

In this section, a one-dimensional particle-in-cell (PIC) simulation is performed to reproduce the relativistic SDA of electrons as discussed above in a self-consistent manner.

In the simulation, a shock is produced by the so-called injection or reflecting wall method. An upstream magnetized plasma is continuously injected from the left-hand boundary. The plasma is reflected at the right-hand boundary and the mixture of the incoming and reflected plasmas results in a downstream medium. The shock is produced at a boundary between the upstream and downstream plasmas. Since the simulation frame is the downstream rest frame, the shock propagates in time from right to left. The simulation is done in the NIF so that the injection flow is parallel to the shock normal, which is along the x-axis. The upstream magnetic field is in the x–z plane. The size of a spatial grid is $\Delta x \approx 0.24\lambda_{De}$ where λ_{De} denotes the electron Debye length, and the number of super particles per cell is $N_p = 200$ for both electrons and ions. Time resolution is $\Delta t = 0.06875\omega_{pe}^{-1}$ where ω_{pe} is the electron plasma frequency. Other physical parameters are shown in Table 1. For Runs A–C, all injection parameters are common except for the shock angle, Θ_{Bn}. The injection Alfvén Mach number is $M_{\rm Ain} = 5$, which results in $M_A \approx 7.8$ or $U_1 \approx 0.061c$ in the shock frame for Run A, for instance, where U_1 denotes the upstream bulk velocity. This value roughly corresponds to the fast Mach number $M_f \approx 2.9$ by using the definition of ion acoustic velocity as $C_s^2 = (3T_i + T_e)/m_i$. The magnetization parameter is $\sigma = 1/9$ and the plasma beta is $\beta = 3(\beta_e = \beta_i)$ so that the upstream electron temperature is ~43 keV. An ion-to-electron mass ratio $m_i/m_e = 1836$ is realistic. In the last two columns, the maximum value of the magnetic field roughly measured in the overshoot relative to the upstream value, B_{os}/B_1, and the associated η_c calculated from Equation (4) are denoted for reference. Note that η_c may in fact be larger if non-negligible potential effects are taken into account (Wu 1984). The most efficient electron acceleration is observed in Run A as expected since $U_1 \tan\Theta_{Bn}/c$ is the largest, although in all cases reflected electrons are seen. Run D is performed with more realistic parameters where $M_{\rm Ain}(= 3)$ and $\sigma(= 1/16)$ are reduced. The results of Run D are essentially the same as those of Run A and are discussed in Section 4. In the following, the results of Run A are discussed.

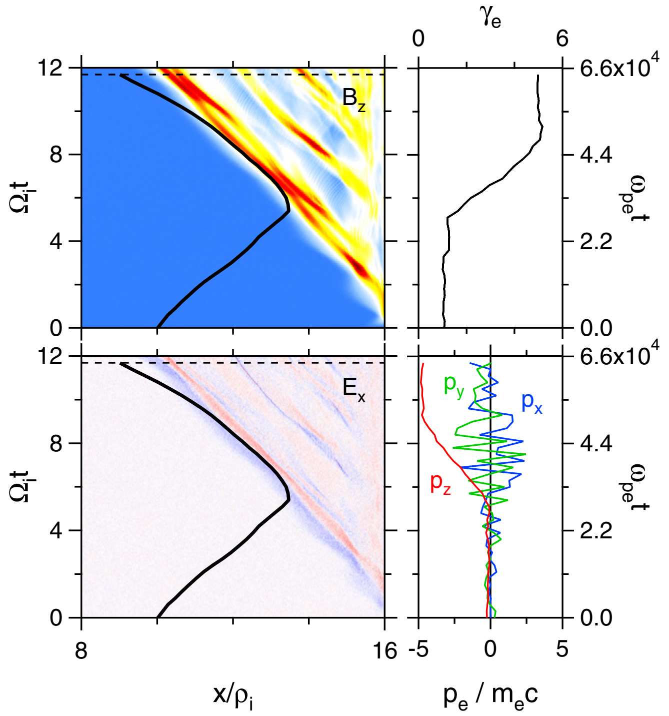

Figure 2. Left: spatiotemporal evolutions of color coded B_z (upper) and E_x (lower) field components and a trajectory of a typical reflected electron. Right: energy (upper) and momentum (lower) histories of the traced electron.

(A color version of this figure is available in the online journal.)

3.1. Run A

In Figure 2, spatiotemporal evolutions of B_z and E_x fields are shown in the left panels. The structure of the shock is more or less time stationary, although it represents weak breathing features (Comisel et al. 2011). An identical trajectory of one of the reflected electrons is denoted as the black solid lines. Its energy (upper) and momentum (lower) time histories are plotted in the right panels. Here, a rate of output data points has been significantly reduced, otherwise p_x (blue) and p_y (green) lines fill in the area because of rapid gyro motions. The electron gains energy mainly through p_z, which is almost parallel to the magnetic field during its stay in the shock transition region. The time the electron stays in the transition region during the reflection process is $\sim\Omega_i^{-1}$. These are typical features of SDA discussed by Krauss-Varban & Wu (1989) and Krauss-Varban et al. (1989), while energy of the reflected electron here becomes relativistic.

The first three panels from the top in Figure 3 show ion $v_x - x$, electron $p_x - x$, and electron $p_z - x$ phase spaces at $\omega_{pe}t = 64350(\Omega_i t \approx 11.7)$, which is indicated as the dashed lines in Figure 2. It is clear in the third panel that some electrons are reflected basically along the magnetic field and have relativistic energies. The fourth panel represents the $p_\perp - p_\parallel$ phase space of the electrons surrounded by the black square in the third panel. Their energy distribution function is plotted as the black line in the bottom panel. The reflected electrons show a ring-beam feature leading to the non-thermal part of the distribution function. A fraction of the bulk energy density of the incoming ions carried by the reflected electrons, ϵ, is estimated as $\epsilon \approx 0.014$. The gray line in the bottom panel is a downstream distribution function corresponding to the region surrounded by the gray square in the third panel. The high-energy part ($\gamma_e - 1 > 1$) looks non-thermal. Its origin is the

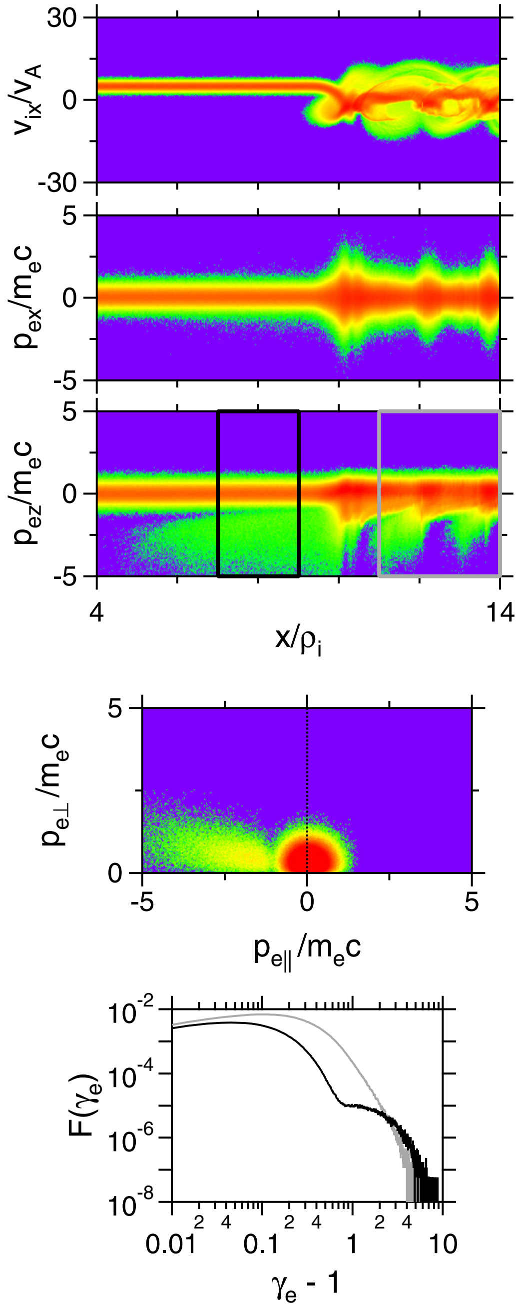

Figure 3. Phase space densities at $\omega_{pe}t = 64350$. The top three panels represent ion $v_x - x$, electron $p_x - x$ and $p_z - x$ phase spaces. The fourth and fifth panels show the $p_\perp - p_\parallel$ phase space and a corresponding energy distribution function of electrons surrounded by the squares in the third panel.

(A color version of this figure is available in the online journal.)

electrons also having large negative p_z around $x/\rho_i \sim 11$ and 13 in the third panel. They are produced in the second and third magnetic overshoots at $x/\rho_i \sim 12$ and 14 seen in Figure 2. By comparing the upstream and downstream energy distribution functions, the highest energy electron is upstream. This implies that in the simulation, the downstream region is still very limited for seeing an equilibrium state and this is clear also from the top three panels.

It is often thought that reflected electrons produce a loss-cone distribution because of their adiabatic behaviors (Lobzin et al. 2005). However, no clear loss-cone is seen in the fourth panel. This is probably due to the effects of small-scale waves generated in the transition region. To avoid getting involved here with a detailed analysis of this problem, we just show evidence of the presence of such small-scale waves. Figure 4 shows B_y field fluctuations in a transition region (upper panel) and its Fourier spectrum at $\omega_{pe}t = 44220$ (lower panel) indicated by the solid line in the upper panel. Tiny streaks in the transition region are visible in the upper panel. They appear in the lower panel as spectral peaks between $0.1 < k\lambda_e < 1$ where $\lambda_e = c/\omega_{pe}$ denotes the electron inertial length. Corresponding structures are also seen in the ion $v_y - x$ phase space indicating that reflected ions destabilize some kind of microinstability (although not shown).

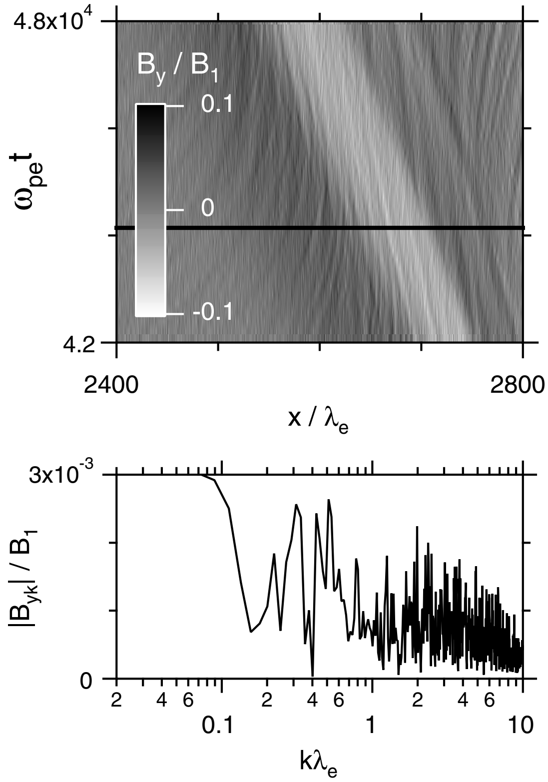

Figure 4. Small-scale fluctuations of B_y in the shock transition region (upper panel) and its Fourier spectrum at $\omega_{pe}t = 44220$ (lower panel).

3.2. *Injection of Reflected Electrons into Further Acceleration Process*

Here, some possible behaviors of the accelerated electrons after being reflected are discussed. Since the reflected electrons form the non-equilibrium distribution function, some local instabilities may be present. However, they may not have been properly treated in the previous section, because there wave vectors only are allowed along the x-axis. In the following, possible instabilities and associated wave-particle interactions are discussed by performing further one-dimensional simulations for various wave propagation angles with periodic boundary conditions. A plasma is assumed to be composed of three components; i.e., incoming electrons and ions and reflected electrons. The reflected electrons are assumed to form a ring-beam distribution with a bulk momentum $(p_{\parallel 0}/m_ec, p_{\perp 0}/m_ec) = (2, 1)$ and a relative density $n_b/n_i = 0.1$, where n_i denotes the density of the incoming ions that are at rest on average. Hence, the simulation is done in the upstream plasma frame of the reference. A density and a bulk momentum of the incoming electrons are

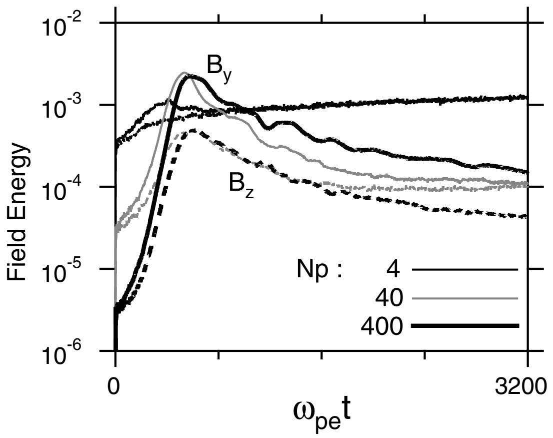

Figure 5. Time histories of B_y (solid lines) and B_z (broken lines) field energies for different numbers of super particles per cell, N_p, in the case of $\theta_{Bk} = 60°$. The black thin, gray thin, and black thick lines denote $N_p = 4, 40$, and 400 cases, respectively.

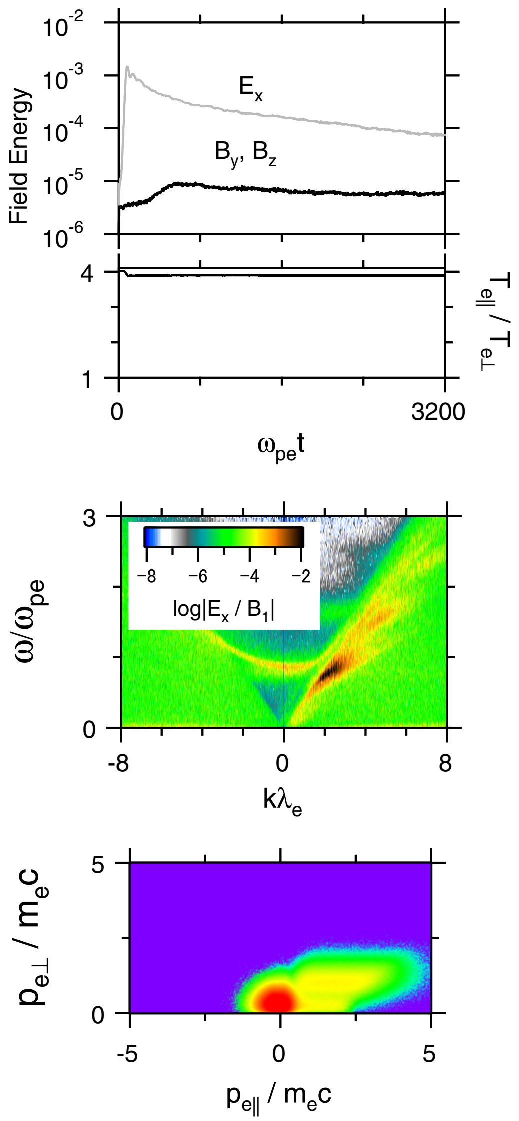

Figure 6. Time histories of field energies (top) and effective electron temperature anisotropy (second), the $\omega - k$ Fourier spectrum of the E_x field for $0 < \omega_{pe}t < 204.8$ (third), and a final electron distribution in the $p_\perp - p_\|$ space (bottom) for $\theta_{Bk} = 0°$.

(A color version of this figure is available in the online journal.)

decided to satisfy charge and current neutral conditions. For all three components, initial temperatures are equal and isotropic in their proper frames. $T/m_ec^2 = \beta_e\sigma/2$, where β_e and σ are chosen to be the same as the values of the upstream plasma in the previous section so that $\beta_e = 1.5$ and $\sigma = 1/9$. The system size is $L/\lambda_e = 819.2$, the number of spatial grids is $N_x = 8192$ corresponding to $\Delta x = 0.1\lambda_e \approx 0.35\lambda_{De}$, the number of super particles per cell is $N_p = 400$, and the time step is $\omega_{pe}\Delta t = 0.1$, respectively. With these parameters fixed, four different runs are performed with various wave propagation angles ($\theta_{Bk} = 0°, 30°, 60°$, and $80°$) with respect to the magnetic field, which is in the x–z plane. Note that θ_{Bk} is independent of the shock angle, Θ_{Bn}.

Before discussing simulation results, we first briefly note how the number of super particles per cell, N_p, is crucial in reproducing a long time evolution of the system. Figure 5 represents evolution of spatially averaged magnetic field energies as a function of time in the $\theta_{Bk} = 60°$ case for three different values of N_p; thin black lines correspond to $N_p = 4$, thin gray lines to $N_p = 40$, and thick black lines to $N_p = 400$, respectively. The solid and broken lines indicate B_y and B_z components. Because of the large noise level, $N_p = 4$ causes totally different results from others. For $N_p = 40$, early development of an instability appears to be calculated properly. However, nonlinear evolution of the system ($\omega_{pe}t > 1000$) may not be well described. In contrast to the case with $N_p = 400$, the B_z component settles in a constant value after $\omega_{pe}t = 1600$ and this at last results in the same level of magnitude as the B_y component. For such an oblique propagation angle, B_z can easily couple with electrostatic fluctuations. The lower limit of B_z field energy in this nonlinear stage may be an influence of electrostatic noise. We confirmed that the results are qualitatively common for $N_p \geqslant 100$, at least up to the time to be discussed below. In the following, results for $N_p = 400$, which we believe to be reliable, will be discussed.

Figure 6 represents the time histories of field energies (top) and effective electron temperature anisotropy (second), the $\omega - k$ spectrum of the E_x field for $0 \leqslant \omega_{pe}t \leqslant 204.8$ (third), and electron distribution in the $p_\perp - p_\|$ phase space at $\omega_{pe}t = 3200$, respectively, for $\theta_{Bk} = 0°$. Here, the effective electron temperature anisotropy is defined as $T_{e\|}/T_{e\perp} \equiv \Sigma_j n_j p_{j\|}^2 / \Sigma_j n_j p_{j\perp}^2$, where the summation is taken over all the incoming and reflected electrons. The rapid growth of E_x field energy is essentially due to the beam (two-stream) instability in which the electron beam destabilizes mainly Langmuir waves and their higher harmonics, as shown in the third panel. Although the electron distribution function forms a plateau in $p_\|$ in the end of the run as seen in the bottom panel, the temperature anisotropy still persists (second panel). Because of the small electromagnetic field energies throughout the run (E_y and E_z field energies are in the noise level), the above process is essentially electrostatic. Electrostatic wave activities are again dominant for $\theta_{Bk} = 30°$, although their intensity is much less than the case with $\theta_{Bk} = 0°$ (not shown).

In contrast, electromagnetic fluctuations become predominant for $\theta_{Bk} \geqslant 60°$. A similar plot to Figure 6 for $\theta_{Bk} = 60°$ is shown in Figure 7, although the third panel is the $\omega - k$ spectrum of the B_y field for $0 \leqslant \omega_{pe}t \leqslant 3276.8$. This electromagnetic instability is essentially of a non-resonant type, which is confirmed from the natural modes of the beam electrons in

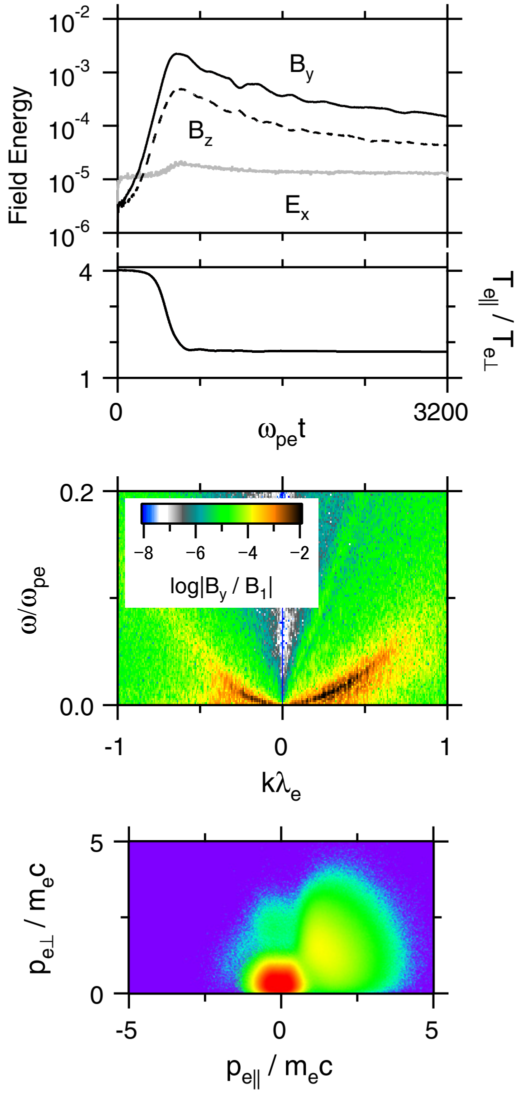

Figure 7. Time histories of field energies (top) and effective electron temperature anisotropy (second), the $\omega - k$ Fourier spectrum of the B_y field for $0 < \omega_{pe}t < 3276.8$ (third), and a final electron distribution in the $p_\perp - p_\|$ space (bottom) for $\theta_{Bk} = 60°$.

(A color version of this figure is available in the online journal.)

the $\omega - k$ spectrum (along $\omega \approx kv_{x0}$ (v_{x0} is a projection of a parallel bulk velocity into the x-direction)) and has no significant intensities in the third panel. They are probably related to one of the oblique modes discussed by Bret (2009), although a detailed linear analysis of kinetic relativistic ring-beam instabilities in a magnetized plasma should be reported elsewhere. The non-resonant instabilities more efficiently relax electron temperature anisotropy (second panel) than the electrostatic beam instability. This is also confirmed by the widely scattered ring-beam electrons in the $p_\perp - p_\|$ space in the bottom panel. In particular some of the ring-beam electrons have a negative $p_\|$. This means that some of the reflected electrons are back scattered by the self-generated waves. (More precisely, electrons having $v_\| \cos\Theta_{Bn} < v_{sh}$ can be regarded as being back scattered (v_sh denotes the shock velocity), although we have not specified here the value of Θ_{Bn}.) Some typical trajectories of the back scattered electrons are shown as solid lines in the top left panel of Figure 8 in which the background gray scale denotes the amplitude of the magnetic fluctuation $|\mathbf{B} - \mathbf{B_0}|$, where $\mathbf{B_0}$ is the ambient magnetic field. While all the electrons initially propagate

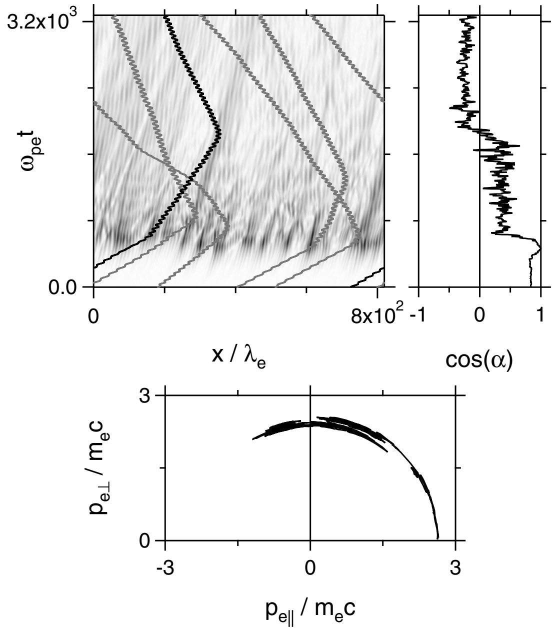

Figure 8. Trajectories of some electrons back scattered by self-generated waves with the background gray scale of amplitudes of magnetic fluctuations (top left). The evolution of the pitch angle cosine (top right) and the trajectory in the $p_\perp - p_\|$ space (bottom) of the black particle in the top left panel are also shown.

in the positive x-direction, they finally have negative velocities in x. The time evolution of the pitch angle cosine of the electron corresponding to the black solid line is plotted in the top right panel and its trajectory in the $p_\perp - p_\|$ space is indicated in the bottom panel. Major changes in the pitch angle cosine occur in two bounded time domains where the electron encounters large amplitude wave packets ($\omega_{pe}t \sim 500$ and ~ 1800). In most of the remaining time, the electron propagates in one direction, although rapid changes in its pitch angle exist. These features are common for all other trajectories in the top left panel.

For $\theta_{Bk} = 80°$, a non-resonant instability is again dominant (not shown). In such large θ_{Bk} generated waves are almost non-propagating pure growing modes, which are the basic features of the Weibel instability. However, the growth time is much longer and the relaxation of the effective electron temperature anisotropy is less efficient than in the $\theta_{Bk} = 60°$ case.

4. SUMMARY AND DISCUSSIONS

It was shown by using a one-dimensional electromagnetic full particle simulation that the relativistic SDA of electrons is feasible even though the quasi-perpendicular shock is rather moderate when the upstream electron temperature becomes of the order of 10 keV or the magnetization parameter σ is not too small (Equation (5)). Such a condition may be realized in large-scale shocks of galaxy clusters, cosmic-ray-modified subshocks of SNRs, etc. For instance, van Weeren et al. (2010) showed evidence of strong acceleration of relativistic electrons forming radio relics in the merging galaxy cluster CIZA J2242.8+5301, where an average temperature of the intracluster medium is estimated as ~9 keV. Their polarization analysis indicates that the observed shock in the radio relics is quasi-perpendicular.

The maximum energy of the reflected electrons is affected by the de Hoffmann–Teller velocity, $V_{\rm HT} = U_1 \tan\Theta_{Bn}$, which is a strong function of the shock angle. The Lorentz transformations derive the energy of a reflected electron as $\gamma_{\rm ref} = \gamma\Gamma_{\rm HT}^2(1+\beta_{\rm HT}^2-$

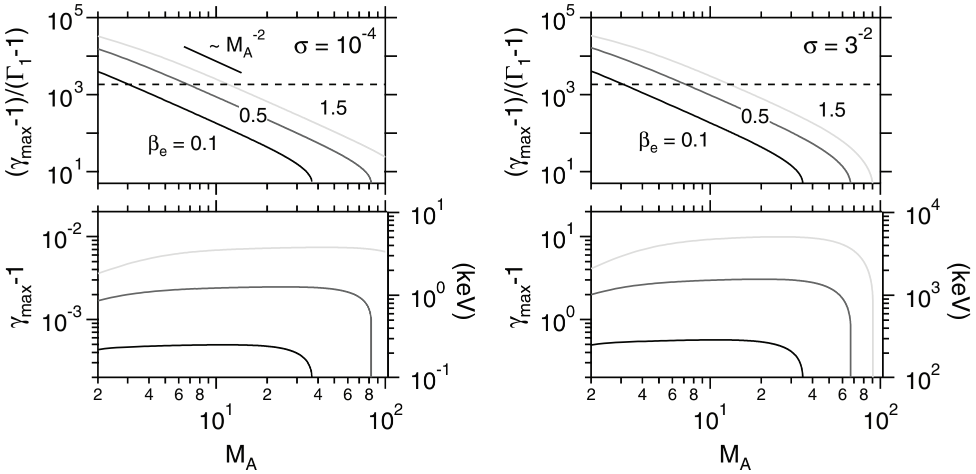

Figure 9. Parameter dependence of the maximum energy through the SDA. The upper panels show the maximum attainable energy of the reflected electrons along the upper edges of the possible reflection areas indicated in Figure 1 normalized to the bulk flow energy of the upstream electrons. The dashed lines denote the bulk energy of the upstream ion flow. The lower panels represent the corresponding Lorentz factor (left axes) and energy in keV (right axes). The line colors indicate different β_e (black: 0.1; dark gray: 0.5; light gray: 1.5). The left and right panels correspond to $\sigma = 10^{-4}$ and 3^{-2}, respectively.

$2\beta_{\rm HT} v_z/c)$, where γ and v_z denote the electron's initial NIF Lorentz factor and velocity component in the z-direction in the shock frame, and $\Gamma_{\rm HT} = (1 - \beta_{\rm HT}^2)^{-1/2}$, $\beta_{\rm HT} = V_{\rm HT}/c$, respectively. When the non-relativistic limit with a large Θ_{Bn} ($\sim 90°$) is considered, the above expression reduces to Equation (16) in Krauss-Varban & Wu (1989). Observed values of the maximum Lorentz factors of upstream electrons for Runs A–C are ∼10.0, ∼4.1, and ∼2.7, respectively. They roughly coincide with the values derived from the above estimate, ∼9.6, ∼3.6, and ∼2.3, where $\gamma \sim 1.9$ (at a maximum) and $v_z/c \sim -0.8$ are again from the simulation. Possible reasons for the underestimation may be neglecting a temporal variation of the shock velocity and/or non-adiabatic features based on the small-scale waves in the transition region.

The parameter dependence of the maximum attainable energy through the SDA is shown in Figure 9. The energies of the reflected particles along the edges of the possible reflection areas in the top two panels in Figure 1 are plotted. Each line color corresponds to different β_e (black: 0.1; dark gray: 0.5; light gray: 1.5). The upper panels show energies of the reflected electrons normalized to upstream electron bulk flow energies. The dashed lines denote the bulk energy of the ion flow. The normalized energies indicate apparent M_A^{-2} dependence for a wide range of M_A. This is consistent with the result that the obtained energies do not basically depend on M_A as confirmed in the lower panels. This is due to the fact that $V_{\rm HT}$ is roughly constant along the edges of the possible reflection area. However, the maximum energy strongly depends on σ implying that the magnetic field strength is crucial. Indeed, it should be noted that the vertical axes in the lower right panel are three orders of magnitude larger than those in the lower left panel, while a ratio of σ between these two panels is also $\sim 10^3$.

The reflected electrons are accelerated mainly in the z-direction, which is almost along the magnetic field, forming the non-thermal part of the energy distribution function upstream of the shock. The efficiency of the energy transfer to the reflected electrons is highest in Run A. If an injection rate, ϵ, is defined as the fraction of energy density carried by the reflected electrons with respect to the bulk energy density of the incoming ions, $\epsilon \approx 1.4\%$ in this case. The corresponding relative number density of the reflected electrons, or the reflection ratio, is 2.6%. These values are to be compared with observations. Finoguenov et al. (2010) estimated that the total energy of radio-emitting electrons in the radio relic in A3667 is 0.15% of the shock kinetic energy, where they adopt the field strength $B \approx 3\,\mu$G to explain dim inverse-Compton emission in the X-ray band. Another observational estimation of the injection efficiency is obtained assuming the equipartition between the energies of the magnetic field and the radio-emitting electrons. Using the observed quantities given in Finoguenov et al. (2010), we derive that 4% of the shock kinetic energy goes into that of radio-emitting electrons. The injection efficiency of a few percent obtained by our simulation result is comparable to the observational estimation (0.1%–4%), which, however, contains various uncertainties. It should be noted that the result here is originated from the one-dimensional simulations only for the particular parameter set and that the injection efficiency depends on various parameters such as the electron temperature, the shock normal angle, etc. To estimate the injection efficiency more accurately, we should perform a detailed survey on parameters as well as two- or three-dimensional simulations, which will be addressed in future works.

The accelerated relativistic-reflected electrons form a non-equilibrium local ring-beam-like distribution function upstream of the shock. It is possible to generate large amplitude waves through a variety of microinstabilities. Local simulations with periodic boundary conditions reveal that the electrostatic electron beam instability is rapidly destabilized basically along the magnetic field. This instability quickly saturates by forming a plateau of the distribution function so that the effective temperature anisotropy ($T_{e\parallel}/T_{e\perp} > 1$) remains. Afterward, the oblique non-resonant instability grows slowly, leading to efficient relaxation of the temperature anisotropy. In this process some of the reflected electrons are scattered back toward the shock by self-generated coherent wave packets. A sequence of the above process, i.e., the reflection of some incoming electrons through the SDA process followed by excitation of the microinstabilities and the backscattering of a part of the reflected electrons by the self-generated waves, may be the first step of injection into the diffusive shock acceleration process.

In Runs A, B, and C, M_A and T_e may be somewhat higher than those of typical large-scale shocks in galaxy clusters. Therefore, an additional Run D is performed to confirm that a similar process can work also for more realistic parameters. Here,

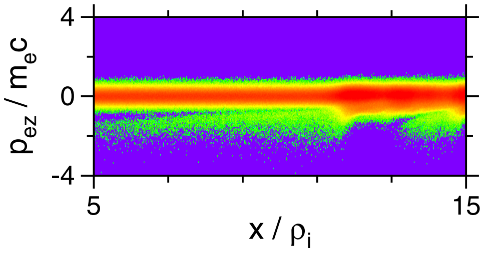

Figure 10. Electron phase space density in $p_z - x$ at $\omega_{pe}t = 85200$ for Run D. (A color version of this figure is available in the online journal.)

$M_A \approx 5.0 (U_1 \approx 0.029c)$, $T_e \approx 24.0$ keV, and $\sigma = 0.0625$ as shown in Table 1. Results are qualitatively similar to Run A. The relativistic SDA works and associated ring-beam electrons are produced upstream. However, the maximum Lorentz factor of the reflected electrons, $\gamma_{\rm ref}^{\rm max} \sim 4$, is not as large as in Run A, since $V_{\rm HT}$ and the initial γ are a little less because of the small M_A and T_e here (Figure 10). In addition, the reflection rate of the incoming electrons becomes smaller, because $\eta_c \approx 1.4$, which is larger than $\eta_c \approx 0.99$ in Run A. Nevertheless, the relativistic SDA can work in such a parameter regime too. In practice, the process may occur even for more moderate and lower temperature shocks if a halo electron component is present in an intracluster medium as in the solar wind (Štverák et al. 2009; Louarn et al. 2009).

In this paper, the effects of higher spatial dimensions have been excluded. We expect that the processes discussed separately in Sections 3.1 and 3.2 are simultaneously observed in two- or three-dimensional systems. However, details of the competing processes among them have been unknown. For example, the electron beam instability is accompanied by pitch angle scattering through multidimensional wave-particle interactions in its nonlinear stage (e.g., Pavan et al. 2009). If this process proceeds more rapidly than the growth of the oblique non-resonant instability, the relaxation of the effective temperature anisotropy and associated backscattering of a part of the reflected electrons might occur. We are also curious to know some other effects like rippling and upstream turbulence (Guo & Giacalone 2010). All these are future issues.

We thank Hiroki Akamatsu and Susumu Inoue for useful comments and discussions. This work was supported by Grant-in-Aid for Scientific Research on Innovative Areas 21200050, Grant-in-Aid for Scientific Research on Priority Areas 19047004 (R.Y.), and Grant-in-Aid for Young Scientists (B) 21740184 (R.Y.) and 22740323 (S.M.).

Note added in proof. Dr. Yutaka Fujita kindly pointed out that upstream temperature may be 1 keV or slightly less near the periphery of the cluster. However, even in this case, $\sqrt{\sigma\beta_e}$ is around unity, so that the electron drift acceleration may occur according to the discussion in Section 2.2.

REFERENCES

Amano, T., & Hoshino, M. 2007, ApJ, 661, 190
Amano, T., & Hoshino, M. 2009, ApJ, 690, 244
Amano, T., & Hoshino, M. 2010, Phys. Rev. Lett., 104, 181102
Bamba, A., Yamazaki, R., Ueno, M., & Koyama, K. 2003, ApJ, 589, 827
Blandford, R. D., & Eichler, D. 1987, Phys. Rep., 154, 1
Bret, A. 2009, ApJ, 699, 990
Cargill, P. J., & Papadopoulos, K. 1988, ApJ, 329, L29
Comisel, H., Scholer, M., Soucek, J., & Matsukiyo, S. 2011, Ann. Geophys., 29, 263
Dieckmann, M. E., McClements, K. G., Chapman, S. C., Dendy, R. O., & Drury, L. O. C. 2000, A&A, 356, 377
Enßlin, T. A., Biermann, P. L., Klein, U., & Kohle, S. 1998, A&A, 332, 395
Feldman, W. C., Anderson, R. C., Bame, S. J., et al. 1983, J. Geophys. Res., 88, 96
Ferrari, C., Govoni, L., Schindler, S., Bykov, A. M., & Rephaeli, Y. 2008, Space Sci. Rev., 134, 93
Finoguenov, A., Sarazin, G. L., Nakazawa, K., Wik, D. R., & Clarke, T. E. 2010, ApJ, 715, 1143
Fujita, Y., Kohri, K., Yamazaki, R., & Kino, M. 2007, ApJ, 663, L61
Fujita, Y., & Sarazin, C. L. 2001, ApJ, 563, 660
Gabici, S., & Blasi, P. 2003, ApJ, 583, 695
Govoni, F., & Feretti, L. 2004, Int. J. Mod. Phys. D, 13, 1549
Guo, F., & Giacalone, J. 2010, ApJ, 715, 406
Hoshino, M., & Shimada, N. 2002, ApJ, 572, 880
Inoue, S., Sigl, G., Miniati, F., & Armengaud, E. 2008, in Proceedings of the 30th ICRC (2007), ed. R. Caballero et al. (Vol. 4; Mexico City: Universidad nacional Autonoma de Mexico), 555
Kang, H., Rachen, J. P., & Biermann, P. L. 1997, MNRAS, 286, 257
Kang, H., Ryu, D., Cen, R., & Ostriker, J. P. 2007, ApJ, 669, 729
Keshet, U., Waxman, E., & Loeb, A. 2004, ApJ, 617, 281
Koyama, K., Petre, R., Gotthelf, E., et al. 1995, Nature, 378, 255
Krauss-Varban, D., & Burgess, D. 1991, J. Geophys. Res., 96, 143
Krauss-Varban, D., Burgess, D., & Wu, C. S. 1989, J. Geophys. Res., 94, 15089
Krauss-Varban, D., & Wu, C. S. 1989, J. Geophys. Res., 94, 15367
Leroy, M. M., & Mangeney, A. 1984, Ann. Geophys., 2, 449
Levinson, A. 1992, ApJ, 401, 73
Lobzin, V. V., Krasnoselskikh, V. V., Schwartz, S. J., et al. 2005, Geophys. Res. Lett., 32, L18101
Louarn, P., Diéval, C., Génot, V., et al. 2009, Sol. Phys., 259, 311
Matsukiyo, S. 2010, Phys. Plasmas, 17, 042901
Miniati, R., Jones, T. W., Kang, H., & Ryu, D. 2001, ApJ, 562, 233
Miniati, R., Ryu, D., Kang, H., et al. 2000, ApJ, 542, 608
Morlino, G. 2009, Phys. Rev. Lett., 103, 121102
Nakar, E., Milosavljević, M., & Nagai, D. 2008, ApJ, 675, 126
Ohira, Y., Murase, K., & Yamazaki, R. 2011, MNRAS, 410, 1577
Ohira, Y., & Takahara, F. 2007, ApJ, 661, L171
Ohira, Y., & Takahara, F. 2008, ApJ, 688, 320
Oka, M., Terasawa, T., Fujimoto, M., et al. 2009, Earth Planets Space, 61, 603
Oka, M., Terasawa, T., Seki, Y., et al. 2006, Geophys. Res. Lett., 33, L24104
Pannuti, T. G., Allen, G. E., Filipović, M. D., et al. 2010, ApJ, 712, 1492
Papadopoulos, K. 1988, Astrophys. Space Sci., 144, 535
Pavan, J., Ziebell, L. F., Gaelzer, R., & Yoon, P. H. 2009, J. Geophys. Res., 114, A01106
Riquelme, M. A., & Spitkovsky, A. 2010, ApJ, 717, 1054
Ryu, D., Kang, H., Hallman, E., & Jones, T. W. 2003, ApJ, 593, 599
Shimada, N., & Hoshino, M. 2000, ApJ, 543, L67
Shimada, N., Terasawa, T., Hoshino, M., et al. 1999, Astrophys. Space Sci., 264, 481
Štverák, Š., Maksimovic, M., Trávníček, P., et al. 2009, J. Geophys. Res., 114, A05104
Tidman, D., & Krall, N. A. 1971, Shock Waves in Collisionless Plasmas (New York: Wiley-Interscience)
Umeda, T., Yamao, M., & Yamazaki, R. 2008, ApJ, 681, L85
Umeda, T., Yamao, M., & Yamazaki, R. 2009, ApJ, 695, 574
van Weeren, R. J., Röttgering, H. J. A., Brüggen, M., & Hoeft, M. 2010, Science, 330, 347
Willson, M. A. G. 1970, MNRAS, 151, 1
Wu, C. S. 1984, J. Geophys. Res., 89, 8857
Wu, C. S., Winske, D., Zhou, Y. M., et al. 1984, Space Sci. Rev., 37, 63